
Vector Space of Cycles

Moo K. Chung¹

Anass B. El-Yaagoubi²

Hernando Ombao²

¹Department of Biostatistics and Medical Informatics, University of Wisconsin, Madison, Wisconsin, USA

²Statistics Program, King Abdullah University of Science and Technology, Thuwal, Saudi Arabia

Abstract

Most statistical and machine learning methods for directed interactions focus on pairwise effects among variables. Even existing cyclic models represent feedback primarily through node-level dependencies, making large-scale recurrent organization difficult to estimate and compare. This limitation is particularly acute in biological and neural systems, where interactions are highly recurrent and involve many overlapping cycles.

We introduce a variational framework for statistical inference on cyclic interactions. Directed interactions are represented as edge flows on a simplicial complex and evolved under an energy-minimizing dynamical system. The resulting dynamics separate transient interaction components from persistent harmonic flows, yielding a low-dimensional cycle space that captures stable recurrent organization. Rather than enumerating individual cycles, the proposed framework represents cyclic interactions as elements of a Hilbert space, enabling projection, averaging, comparison, and population-level statistical inference.

We establish theoretical properties of the harmonic projection, including characterization of the cycle space, variance reduction, and population inference. Simulations demonstrate substantially improved recovery of cyclic structure in dense recurrent systems compared with existing directed-interaction methods. Applied to resting-state fMRI from 400 human subjects, the framework reveals reproducible large-scale cyclic organization that is not detectable through edgewise averaging. These results provide a scalable statistical framework for studying recurrent interactions in high-dimensional dynamical systems.

1 INTRODUCTION

Many statistical and machine learning methods for directed interactions are built on regression, conditional independence, and structural equation models defined on nodes [Pearl, 2009, Peters et al., 2017, Spirtes et al., 2000]. These approaches have achieved considerable success in estimating pairwise directional relationships, particularly in systems that are sparse and weakly coupled. However, many real-world systems—including biological, neural, social, and economic networks—are dominated by recurrence, feedback, and large numbers of interacting cycles [Anand and Chung, 2023, Forré and Mooij, 2018]. In such settings, the primary organizational structure is often not an individual directed edge but a collection of interacting cyclic pathways. Existing methods typically represent cycles indirectly through node-level dependencies, making large-scale recurrent organization difficult to estimate, compare, and statistically analyze.

This limitation motivates a different perspective. Rather than treating cycles as secondary structures to be inferred from collections of directed edges, we treat cyclic interactions as primary objects of inference. We propose a variational framework in which directed interactions are represented as edge flows evolving on a simplicial complex. The evolution is governed by an energy-minimizing dynamical system that separates transient interaction components from persistent recurrent organization. Cyclic interactions emerge as stable harmonic flows that persist under the dynamics, while non-cyclic and energetically inconsistent components dissipate over time. This formulation shifts the inferential target from node-to-node relationships to edge-to-cycle organization.

The proposed framework provides a coherent mathematical and statistical representation of cyclic interactions. In the strongly overdamped regime, the dynamics reduce to Dirichlet–Hodge diffusion [Chung et al., 2026, Schaub et al., 2020], which separates directed interactions into transient and persistent components. The persistent component lies in a low-dimensional harmonic subspace, providing a vector-

space representation of admissible cycles. This avoids explicit cycle enumeration and enables projection, averaging, comparison, and inference through linear operations in a Hilbert space.

Related work. Our work is related to four lines of research on recurrent interactions and cycles.

Classical graph-theoretic methods characterize networks through pairwise measures such as degree, clustering, modularity, path length, and centrality [Sporns et al., 2000]. Cycles are typically treated indirectly through path redundancy, strongly connected components, or explicit cycle enumeration algorithms [Tarjan, 1972, Johnson, 1975]. While effective for small networks, explicit cycle recovery becomes computationally challenging in dense recurrent systems containing many overlapping feedback loops.

Persistent homology and topological data analysis (TDA) study cycles through homological invariants across filtration scales [Lee et al., 2014, Chung et al., 2019]. These methods detect the presence and persistence of cycles but do not directly model directed interaction flows. Hodge-theoretic methods decompose edge flows into gradient, curl, and harmonic components [Lim, 2020, Schaub et al., 2020, Anand and Chung, 2023, Su et al., 2024], but existing applications have mainly focused on flow decomposition and network characterization. In contrast, we represent cyclic interactions as elements of a harmonic vector space, enabling projection, averaging, comparison, and population-level inference for recurrent organization.

Our work is also related to directed interaction models, including Granger causality, structural equation models, transfer entropy, and Bayesian network methods [Granger, 1969, Driver et al., 2017, Schreiber, 2000]. Cyclic structural causal models allow feedback among variables [Richardson, 1996, Lacerda et al., 2008, Mooij et al., 2013, Bongers et al., 2021, Forré and Mooij, 2018], but their inferential target remains node-level dependence, with cycles represented implicitly through edge collections. This representation can be unstable in dense recurrent networks with overlapping feedback loops. In contrast, we treat cyclic interactions as the inferential object and represent them in a harmonic cycle space, enabling stable projection, averaging, comparison, and inference.

Finally, variational and energy-based methods have been widely used to study dynamical systems [Arnol'd, 2013, Goldstein, 1950, Ambrosio et al., 2005]. More recently, Hamiltonian and Lagrangian neural networks have incorporated physical principles into learned dynamical representations [Greydanus et al., 2019, Lutter et al., 2019, C. et al., 2019]. Our objective is different. We employ an energy-minimization principle to identify and separate transient interactions from persistent recurrent organization, yielding a low-dimensional cycle space that supports projection,

averaging, comparison, and population-level statistical inference.

Contributions. Our contributions are fourfold. First, we introduce a variational framework for identifying persistent cyclic interactions in directed networks. Under Dirichlet–Hodge diffusion, transient interaction components dissipate while harmonic flows remain as stable recurrent structures, providing a principled mechanism for separating persistent cyclic organization from transient edgewise fluctuations.

Second, we formulate cyclic interactions as elements of a vector space. Rather than representing cycles as combinatorial objects requiring explicit enumeration, we represent them as harmonic flows in a low-dimensional Hilbert space. This transforms cycle analysis into linear operations such as projection, averaging, and comparison.

Third, we establish statistical properties of the cycle-space representation. We characterize the harmonic subspace, derive variance-reduction properties of harmonic projection, and develop population-level inference based on directional statistics on the harmonic unit sphere.

Finally, we demonstrate the framework in both synthetic and neuroimaging studies. Simulations show substantial improvements in recovering cyclic structure in dense recurrent networks. In resting-state fMRI from 400 Human Connectome Project participants, the proposed method reveals reproducible large-scale cyclic organization that is not detectable by conventional edgewise averaging or acyclic graphical representations [Anand and Chung, 2023]. Although directed interactions vary substantially across time and individuals, their harmonic components exhibit strong population-level alignment, suggesting that persistent cyclic organization forms a stable component of large-scale brain network dynamics.

Scope and limitations. The proposed framework is not intended to replace Pearl–Rubin causal identification or to estimate intervention effects [Pearl, 2009, Peters et al., 2017]. Its target is narrower: statistical inference on persistent cyclic interactions in feedback-dominated dynamical systems. The method assumes that directed edge flows are first estimated from the observed data and then used as input to the proposed energy-minimization principle. Thus, its performance depends on the quality of the initial directed interaction estimates. When the underlying system contains little recurrent structure, or when there is no cycle, the harmonic subspace is trivial and no persistent cyclic organization can be inferred.

2 LAGRANGIAN DYNAMICS

The classical Lagrangian framework [Arnol'd, 2013] describes dynamical systems through an energy-based varia-

tional principle. In conservative systems, such as an ideal pendulum, energy is exchanged between kinetic and potential forms and motion may persist indefinitely. Here, we use this variational viewpoint to model how directed interactions evolve under geometric and topological constraints.

Simplicial complex for encoding interactions. To model higher-order interaction structure, we represent interactions as a simplicial complex consisting of vertices V (0-simplices), edges E (1-simplices), faces F (2-simplices), and higher-dimensional simplices (Figure 1) [Edelsbrunner and Harer, 2010]. This generalizes pairwise graphs by encoding multi-way structure as higher-dimensional simplices, providing a combinatorial scaffold for topological and variational analysis. Given multivariate observations $Z(t)$ at the vertices, we construct a time-varying directed edge flow

$$X(t) \in \mathbb{R}^{|E|},$$

where each component quantifies directed interaction along an oriented edge. The edge flow may be instantiated using any directed interaction measure, including time-lagged dependence, coherence, Granger-type residuals, or transfer entropy [Keilholz et al., 2017, Barnett and Seth, 2014, Peters et al., 2017, Schreiber, 2000]. Thus, the framework is estimator-agnostic and treats $X(t)$ as the input interaction field for subsequent cycle-space analysis.

The topology of the simplicial complex is encoded by boundary matrices $\mathbf{B}_1 \in \mathbb{R}^{|V| \times |E|}$ and $\mathbf{B}_2 \in \mathbb{R}^{|E| \times |F|}$ Anand and Chung [2023], Lim [2020]). Acting on an edge flow, \mathbf{B}_1 measures node-level source–sink imbalance, while \mathbf{B}_2^\top measures circulation around filled faces. These operators define the discrete differential structure used to quantify transient imbalance, local circulation, and persistent global cyclic organization within a unified variational framework.

Lagrangian. We represent directed interactions on a network by a time-dependent *edge flow* $X(t) \in \mathbb{R}^{|E|}$, where each component of $X(t)$ encodes the directed strength of interaction along an edge at time t .

Let $\dot{X}(t) = \frac{d}{dt}X(t)$ denote its time derivative. We define the Lagrangian governing the evolution of the interaction flow as

$$\mathcal{L}(X, \dot{X}) = \frac{1}{2} \|\dot{X}\|_2^2 - \mathcal{E}(X).$$

The first term is a kinetic energy that penalizes rapid temporal changes in the interaction flow, promoting temporal smoothness. The second term is a *Dirichlet potential energy* [Chung and Yau, 1997] induced by the topology of the simplicial complex,

$$\mathcal{E}(X) = \frac{1}{2} X^\top \Delta_1 X,$$

where Δ_1 is the 1-Hodge Laplacian Anand and Chung [2023], Lim [2020], Schaub et al. [2020]),

$$\Delta_1 = \mathbf{B}_1^\top \mathbf{B}_1 + \mathbf{B}_2 \mathbf{B}_2^\top.$$

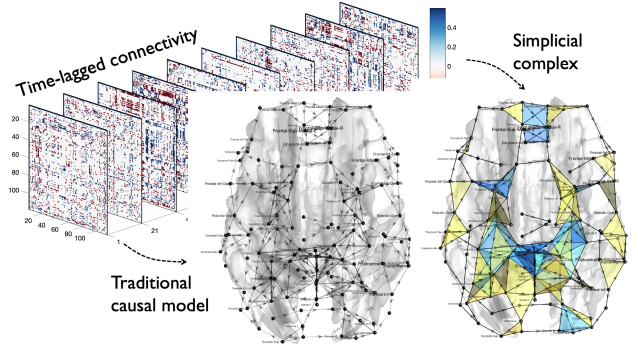


Figure 1: **Left:** Time-lagged dynamic connectivity matrix representing directed interaction dynamics. **Middle:** Conventional directed-network analysis represents pairwise interactions on a graph. **Right:** The proposed framework represents interactions on a simplicial complex encoding nodes, edges, and faces. The topology does not impose cyclic organization *a priori*; persistent cyclic structure is inferred from the observed interaction flow through variational dynamics on this scaffold.

Together, the Lagrangian balances smooth temporal evolution with global topological coherence of the directed interaction flow.

Action. Given the Lagrangian $\mathcal{L}(X, \dot{X})$, the *action* of an edge-flow trajectory $X(t)$ is defined as [Arnol’d, 2013]

$$\mathcal{A}[X] = \int_0^\infty \mathcal{L}(X(t), \dot{X}(t)) dt.$$

The action assigns a scalar cost to the full temporal evolution of the interaction flow, balancing dynamical smoothness with topological coherence. In conservative systems, admissible trajectories are stationary points of the action. Using variational notation δ Arnol’d [2013], this condition is written as

$$\delta \mathcal{A}[X] = 0.$$

The resulting stationary trajectories satisfy the Euler–Lagrange equation governing the temporal evolution of the interaction flow. For the second time derivative $\ddot{X}(t) = \frac{d^2}{dt^2} X(t)$, we have:

Theorem 1 (Euler–Lagrange dynamics of interaction flows). *An edge-flow trajectory $X(t)$ is a stationary point of the action functional $\mathcal{A}[X]$ if and only if it satisfies*

$$\ddot{X}(t) + \Delta_1 X(t) = 0.$$

The Euler–Lagrange equation is classical in mechanical systems; here we extended to directed interaction flows on a simplicial complex. The proof is given in Appendix. The equation describes coupled harmonic oscillators [Arnol’d, 2013] on edges, with coupling determined by the topology

encoded in the 1-Hodge Laplacian Δ_1 . Because the dynamics are conservative, the resulting trajectories are generally oscillatory and need not converge to stable configurations. Thus, conservative variational dynamics alone are insufficient for isolating persistent cyclic organization.

Dissipative dynamics. To obtain stable interaction patterns, we extend the conservative Lagrangian framework by incorporating the Rayleigh dissipation functional [Goldstein, 1950]

$$\mathcal{R}(\dot{X}) = \frac{\gamma}{2} \|\dot{X}\|_2^2,$$

which penalizes rapid temporal variation of edge flows. The associated dissipative force is

$$F = -\frac{\partial \mathcal{R}}{\partial \dot{X}} = -\gamma \dot{X},$$

so larger temporal velocities experience stronger damping. The evolution is governed by the Lagrange–d’Alembert principle [Arnol’d, 2013, Goldstein, 1950],

$$\delta \mathcal{A}[X] = -\int_0^\infty \langle F, \delta X \rangle dt, \quad (1)$$

which balances conservative variational structure with dissipation.

When $\gamma = 0$, this principle reduces to the Euler–Lagrange equation. For $\gamma > 0$, dissipation suppresses rapidly fluctuating interaction components and favors slowly varying, structurally consistent trajectories. Thus, dissipation acts as an intrinsic regularizer on the space of edge-flow trajectories.

Theorem 2 (Dissipative dynamics of interaction flows). *An edge-flow trajectory $X(t)$ satisfies the Lagrange–d’Alembert principle if and only if it satisfies the damped Euler–Lagrange equation*

$$\ddot{X} + \gamma \dot{X} + \Delta_1 X = 0, \quad (2)$$

where $\gamma > 0$ controls the rate at which transient interaction components are dissipated.

The proof is given in Appendix. The damped Euler–Lagrange equation defines coupled damped harmonic oscillators on edges, with coupling determined by the 1-Hodge Laplacian Δ_1 . This edge-based formulation describes how directed interactions propagate and stabilize through cycles. In contrast, using the 0-Hodge Laplacian Δ_0 , the standard graph Laplacian, yields coupled damped oscillators on nodes. Node-based oscillator models are widely used for synchronization and consensus dynamics [Olfati-Saber et al., 2007, Arenas et al., 2008, Mesbahi and Egerstedt, 2010], but they describe state alignment rather than edge-flow circulation and therefore do not represent persistent cyclic interaction patterns.

Emergence of stable cyclic interactions. The damped Euler–Lagrange dynamics (2) exhibit stable long-time behavior. For $\gamma \gg 1$, damping suppresses oscillatory transients and the flow relaxes toward a topology-constrained configuration determined by Δ_1 . In neuronal systems, such stabilization is analogous to inhibitory mechanisms that regulate recurrent excitation and prevent runaway dynamics [Dayan and Abbott, 2005, V.C. and Sompolinsky, 1996]. Consequently, persistent cyclic organization emerges as a stable energy-consistent flow rather than a collection of transient interactions.

To characterize the asymptotic regime, introduce the slow time $\tau = t/\gamma$, so that

$$\frac{d}{dt} = \frac{1}{\gamma} \frac{d}{d\tau}, \quad \frac{d^2}{dt^2} = \frac{1}{\gamma^2} \frac{d^2}{d\tau^2}.$$

Equation (2) becomes

$$\frac{1}{\gamma^2} \frac{d^2 X}{d\tau^2} + \frac{dX}{d\tau} + \Delta_1 X = 0.$$

In the strongly damped regime, the inertial term is $\mathcal{O}(\gamma^{-2})$ and negligible, yielding the first-order approximation

$$\dot{X}(t) = -\frac{1}{\gamma} \Delta_1 X(t).$$

After rescaling time, this reduces to

$$\dot{X}(t) = -\Delta_1 X(t), \quad (3)$$

which we refer to as the *Dirichlet–Hodge diffusion*.

The Dirichlet–Hodge diffusion defines a purely dissipative evolution that monotonically decreases the Dirichlet energy and relaxes the system toward a stable configuration. Unlike conservative dynamics, which may sustain oscillations, the diffusive limit suppresses inertial effects and guarantees convergence to the harmonic component [Anand and Chung, 2024]. The initial interaction flow is progressively regularized by the topology encoded in Δ_1 , so that transient components dissipate while only globally consistent cyclic organization persists in the long-time limit.

Harmonic flows. In the strongly dissipative regime, inertial effects vanish and the evolution is governed solely by the Dirichlet energy

$$\mathcal{E}(X) = \frac{1}{2} X^\top \Delta_1 X.$$

The system therefore evolves by steepest descent of \mathcal{E} in the edge-flow space. By Onsager’s variational principle [Noirhomme et al., 2024], the overdamped limit of the dissipative Lagrangian dynamics yields precisely the Dirichlet–Hodge diffusion introduced above. Along this evolution, the Dirichlet energy serves as a Lyapunov function [Ambrosio et al., 2005]. Differentiating along trajectories gives

$$\frac{d}{dt} \mathcal{E}(X(t)) = -\|\Delta_1 X(t)\|_2^2 \leq 0,$$

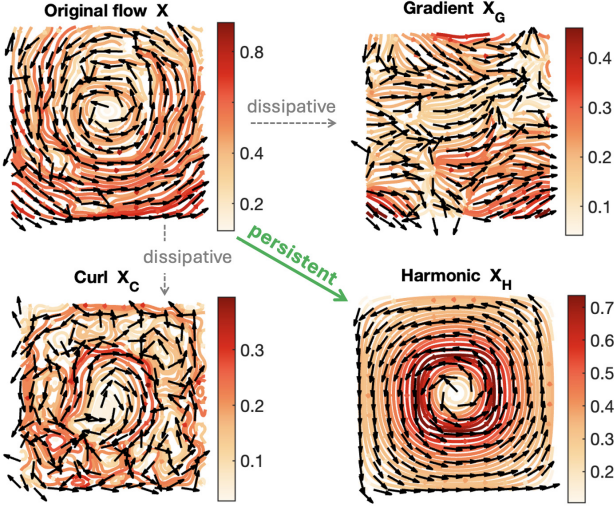


Figure 2: The gradient and curl flows X_G and X_C correspond to dissipative structures of the original flow X that decay under Dirichlet–Hodge diffusion. In contrast, the harmonic flow X_H is non-dissipative and therefore persists under diffusion, encoding the globally consistent, topologically constrained circulation that remains after transient components dissipate.

so the energy decreases monotonically in time. Consequently, all components with positive Dirichlet energy decay, and the trajectory converges to the null space

$$\ker(\Delta_1) = \{X \in \mathbb{R}^{|E|} : \Delta_1 X = 0\}.$$

The limiting configuration is therefore the projection of the initial flow onto $\ker(\Delta_1)$, consisting entirely of non-dissipative modes. These persistent modes define the *harmonic flow*, which emerges intrinsically as the stable cyclic organization of the interaction flow (Figure 2).

3 VECTOR SPACE OF CYCLES

The central object of interest is the harmonic subspace $\ker(\Delta_1)$. We show that the long-time behavior of the Dirichlet–Hodge diffusion naturally leads to a vector-space representation of cyclic interactions in this space.

Limit of Dirichlet–Hodge diffusion. Let $\{\phi_k\}$ be an orthonormal eigenbasis of the 1-Hodge Laplacian Δ_1 with eigenvalues $\lambda_k \geq 0$, satisfying

$$\Delta_1 \phi_k = \lambda_k \phi_k.$$

Expanding the initial interaction flow as

$$X(0) = \sum_k \alpha_k \phi_k, \quad \alpha_k = \phi_k^\top X(0),$$

the solution of the Dirichlet–Hodge diffusion (3) is

$$X(t) = e^{-\Delta_1 t} X(0) = \sum_k e^{-\lambda_k t} \alpha_k \phi_k.$$

As $t \rightarrow \infty$, all modes with $\lambda_k > 0$ decay exponentially, while modes with $\lambda_k = 0$ persist. The limiting flow is therefore

$$X_H = \lim_{t \rightarrow \infty} X(t) = \sum_{\lambda_k=0} \alpha_k \phi_k.$$

Thus, the long-time dynamics automatically filter out dissipative components and retain only the non-dissipative harmonic component.

The limiting harmonic flow can be written as

$$X_H = \mathcal{P}_H X(0),$$

where

$$\mathcal{P}_H = \sum_{\lambda_k=0} \phi_k \phi_k^\top$$

is the orthogonal projection onto the null space

$$\ker(\Delta_1) = \{X \in \mathbb{R}^{|E|} : \Delta_1 X = 0\}.$$

The orthogonal operator \mathcal{P}_H extracts the persistent component of the interaction flow selected by the variational dynamics.

Harmonic subspace as a cycle space. The harmonic subspace $\ker(\Delta_1)$ is a linear subspace of the edge-flow space. Hence, if $X_1, X_2 \in \ker(\Delta_1)$ are harmonic flows and $a, b \in \mathbb{R}$, then

$$\Delta_1(aX_1 + bX_2) = a\Delta_1 X_1 + b\Delta_1 X_2 = 0.$$

Thus, any linear combination of harmonic flows is again harmonic. In particular, adding two admissible cyclic flows produces another admissible cyclic flow. Thus, averaging of cycles are well-defined operations that preserve cyclic consistency (Figure 3).

In contrast, if $X_H \in \ker(\Delta_1)$ is harmonic and $X_D \notin \ker(\Delta_1)$ is non-harmonic, then $X_H + X_D$ is generally non-harmonic because

$$\Delta_1(X_H + X_D) = \Delta_1 X_D \neq 0.$$

In the vector space $\ker(\Delta_1)$, we have well defined inner product between cycles: $\langle X_H, Y_H \rangle = X_H^\top Y_H$, which measures cyclic alignment and similarity between recurrent flow patterns.

Under Dirichlet–Hodge diffusion, this non-harmonic component dissipates, while the harmonic component remains invariant. Equivalently,

$$\mathcal{P}_H(X_H + X_D) = X_H,$$

provided X_D is orthogonal to $\ker(\Delta_1)$. Thus, harmonic projection removes transient non-cyclic components and retains the admissible cyclic component.

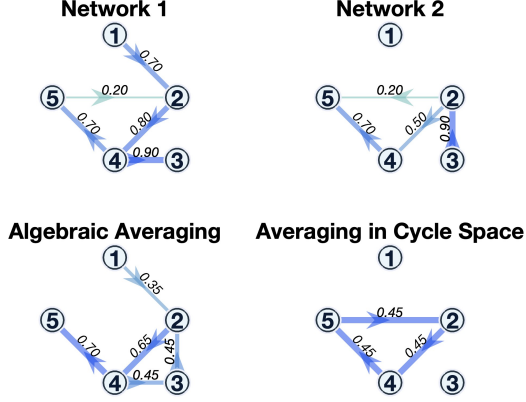


Figure 3: Two networks contain partially inconsistent cyclic structure involving $2 \rightarrow 4 \rightarrow 5$. Direct algebraic averaging removes this cycle and instead introduces a spurious cycle $2 \rightarrow 4 \rightarrow 3$ that is not present in either network. In contrast, averaging in the harmonic cycle space enhances the coherent recurrent cycle $5 \rightarrow 2 \rightarrow 4 \rightarrow 5$.

Theorem 3 (Harmonic flows are cycles). *Every nonzero harmonic flow $X \in \ker(\Delta_1)$ represents a circulation around cycles of the simplicial complex.*

The proof is given in Appendix. Consequently, the harmonic subspace provides a vector-space representation of cyclic interactions: cycles can be added, scaled, averaged, and projected while remaining inside the same admissible cycle space.

The dimension of the harmonic subspace is

$$\dim \ker(\Delta_1) = \beta_1,$$

where β_1 is the first Betti number of the simplicial complex [Edelsbrunner and Harer, 2010]. Therefore, $\ker(\Delta_1)$ is spanned by β_1 independent cycle representatives, and every harmonic flow is a linear combination of these cycles.

Numerical implementation. The boundary matrices \mathbf{B}_1 and \mathbf{B}_2 are highly sparse, with at most two nonzero entries per column in \mathbf{B}_1 and three per column in \mathbf{B}_2 . The harmonic projection does not require explicit eigendecomposition of the Hodge Laplacian, which can be computationally expensive for large complexes. Instead, it is computed via a constrained least-squares formulation, reducing the problem to solving a sparse linear system.

Given an edge flow $X \in \mathcal{C}^1$, we aim to extract its harmonic component $X_H \in \ker(\mathbf{B}_1) \cap \ker(\mathbf{B}_2^\top)$, which lies in the kernel of the Hodge 1-Laplacian. Thus, the harmonic component is the unique solution to the orthogonal projection problem:

$$X_H = \arg \min_{Z \in \mathbb{R}^{|E|}} \|X - Z\|^2 \text{ under } \mathbf{B}_1 Z = 0, \mathbf{B}_2^\top Z = 0.$$

This is a least-squares estimation (LSE) problem with linear equality constraints, projecting X onto the harmonic subspace.

Let \mathbf{B} denote the stacked boundary and coboundary matrix:

$$\mathbf{B} = \begin{bmatrix} \mathbf{B}_1 \\ \mathbf{B}_2^\top \end{bmatrix}.$$

The orthogonal projection onto $\ker(\mathbf{B})$ is given by

$$\mathcal{P}_H = I - \mathbf{B}^\top (\mathbf{B}\mathbf{B}^\top)^\dagger \mathbf{B},$$

where $(\cdot)^\dagger$ denotes the Moore–Penrose pseudoinverse. The harmonic component is then computed as

$$X_H = \mathcal{P}_H X.$$

Variance reduction properties. Harmonic projection improves statistical stability by removing dissipant components and isolating globally persistent cyclic structure. As a result, statistical inference is conducted in a variance-reduced subspace. To quantify this effect, let $X \in \mathbb{R}^{|E|}$ be a random edge flow with covariance Σ_X . We define the total variance

$$\text{Var}(X) = \mathbb{E} \|X - \mathbb{E}X\|_2^2 = \text{tr}(\Sigma_X).$$

Theorem 4 (Variance reduction). *If $\Sigma_X = \sigma^2 I$, then for harmonic flow $X_H = \mathcal{P}_H X$,*

$$\text{Var}(X_H) = \frac{\beta_1}{|E|} \text{Var}(X),$$

where $\beta_1 = \dim \ker(\Delta_1)$ is the first Betti number.

The proof is given in Appendix. Since typically $\beta_1 \ll |E|$, harmonic projection contracts noise by a factor $\beta_1/|E|$, concentrating variability into a low-dimensional topologically constrained subspace. In our human neural network application, this ratio is approximately $534/6670 \approx 0.08$, explaining the empirical stability of the population-level harmonic flow and enabling reliable group-level inference.

Inference in cycle space. For subject s , let

$$X_H^{(s)} = \mathcal{P}_H X^{(s)} \in \ker(\Delta_1)$$

denote the subject-level harmonic flow. The population mean is

$$\mu = \mathbb{E}[X_H^{(s)}],$$

and we test the null hypothesis

$$H_0 : \mu = 0,$$

which asserts the absence of systematic cyclic organization across subjects. Rejection of H_0 indicates population-level alignment of harmonic flows beyond random fluctuation.

Under H_0 , subjects may individually exhibit nonzero harmonic flows, but their directions fluctuate independently and do not align coherently. We therefore focus on directional alignment rather than magnitude. Define the normalized harmonic flow

$$U^{(s)} = \frac{X_H^{(s)}}{\|X_H^{(s)}\|_2} \in \mathbb{S}_H^{\beta_1-1},$$

which lies on the harmonic unit sphere

$$\mathbb{S}_H^{\beta_1-1} = \left\{ U \in \ker(\Delta_1) : \|U\|_2 = 1 \right\}.$$

Population-level cyclic coherence corresponds to concentration of the directions $U^{(s)}$ around a common orientation in the harmonic cycle space (Figure 4).

Alignment across subjects is quantified by the geodesic distance induced by cosine similarity [Luo et al., 2018, Zhao and Jia, 2025]:

$$\theta_{st} = \cos^{-1}(\langle U^{(s)}, U^{(t)} \rangle),$$

which measures the angular separation between subjects s and t . Because cosine similarity depends only on orientation, it is invariant to scale and measures directional agreement independently of magnitude.

The sample mean direction is

$$\bar{U} = \frac{1}{n} \sum_{s=1}^n U^{(s)}.$$

Its norm $\|\bar{U}\|_2$ measures directional concentration across subjects: random orientations cancel so that \bar{U} is close to zero, whereas coherent cyclic organization yields larger $\|\bar{U}\|_2$.

Inference is performed using the Rayleigh test for mean direction [Mardia and Jupp, 2009]. Since the harmonic flows are restricted to the β_1 -dimensional cycle space $\ker(\Delta_1)$, the relevant dimension is β_1 , not the ambient edge dimension $|E|$. Under H_0 , the normalized directions are uniformly distributed on $\mathbb{S}_H^{\beta_1-1}$. By rotational symmetry,

$$\mathbb{E}[U^{(s)}] = 0, \quad \text{Cov}(U^{(s)}) = \frac{1}{\beta_1} I_{\beta_1}.$$

By the multivariate central limit theorem [Casella and Berger, 2024],

$$\sqrt{n} \bar{U} \xrightarrow{d} N\left(0, \frac{1}{\beta_1} I_{\beta_1}\right).$$

Therefore,

$$\beta_1 n \|\bar{U}\|_2^2 \xrightarrow{d} \chi_{\beta_1}^2.$$

The corresponding p -value is

$$p = \mathbb{P}(\chi_{\beta_1}^2 \geq \beta_1 n \|\bar{U}\|_2^2).$$

A significant result indicates reproducible cyclic organization across subjects in the harmonic cycle space.

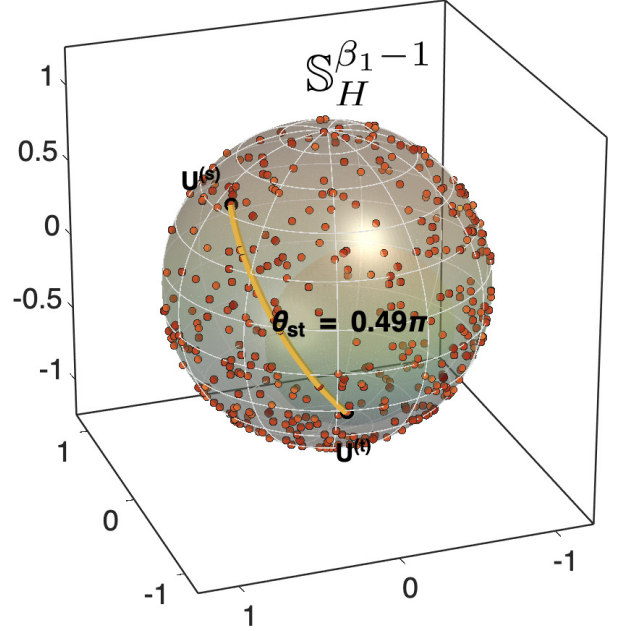


Figure 4: Normalized harmonic flows from 400 subjects lie on $\mathbb{S}_H^{\beta_1-1}$ and are embedded onto S^2 using spherical MDS for visualization. The arc shows the geodesic angle θ_{st} , where $\cos \theta_{st} = \langle U^{(s)}, U^{(t)} \rangle$.

4 VALIDATION

Our validation focuses on recovering cyclic interactions, the inferential target of this paper. Accordingly, the synthetic studies evaluate recovery of cyclic ground truth. We compare the proposed framework against six representative directed-interaction baselines spanning temporal prediction, instantaneous structural modeling, information-theoretic dependence, lagged correlation, DAG-constrained optimization, and cyclic constraint-based discovery: Granger causality [Granger, 1969], SEM [Driver et al., 2017], Bayesian MAP SVAR [Lütkepohl, 2005, Kilian and Lütkepohl, 2017], transfer entropy [Schreiber, 2000], lagged Pearson correlation [Smith et al., 2011, Keilholz et al., 2017], NOTEARS [Zheng et al., 2018], and CCD [Richardson, 1996].

We will make the full simulation code and random cubical-complex simulation toolbox publicly available upon publication.

Ground Truth. We generate cyclic ground truth using random cubical complexes [Chung et al., 2024], which provide directed edge flows with known recurrent structure for evaluating cyclic recovery (Fig. 5, left). We construct a directed 1-skeleton on a 5×5 cubical grid, where nodes correspond to lattice vertices and edges connect horizontally and vertically adjacent vertices. Directed interactions are assigned along the boundaries of selected square faces to induce coherent circulations, producing a nontrivial harmonic subspace.

Clockwise (red) and counterclockwise (blue) circulations define the embedded ground-truth cyclic interactions, providing known cycle orientations and strengths against which estimated harmonic flows can be quantitatively compared.

Time series data at each node are simulated so that their dependencies follow the prescribed ground-truth edge flows. We then generate a vector autoregressive (VAR) process of order L [Gong et al., 2024, Papana et al., 2017, Primiceri, 2005]:

$$Z_t = \sum_{\ell=1}^L A_\ell Z_{t-\ell} + \varepsilon_t, \quad \varepsilon_t \sim N(0, \sigma^2 I),$$

where $Z_t \in \mathbb{R}^{|V|}$ represents node-level activity at time t . The lag matrices A_ℓ are constructed directly from the ground-truth edge-flow matrix $W = (w_{ij})$, where w_{ij} encodes the directed interaction strength from node i to node j . For each lag, $A_\ell = \rho I + c \delta^{\ell-1} W$, where $\rho = 0.1$ controls self-retention (the extent to which each node preserves its own past activity), $c = 0.1$ scales interaction strength along directed edges, and $\delta = 0.5$ imposes geometric decay across higher-order lags. For each simulation, 200 time points are generated. A relatively long lag order ($L = 10$) disperses the direct cyclic influence across time, blurring immediate feedback structure and making recovery of the underlying cyclic interactions substantially more challenging.

The reported ground truth configuration is representative, and all results are based on 100 independent trials with independently generated noise (three settings $\sigma = 0.1, 1, 10$) and time series. The synthetic data-generation process does *not* use any component of the proposed method. All methods are blind to the ground truth cyclic information. Thus, although the evaluation target is cyclic by design, the data-generating mechanism is independent of the proposed method.

We performed stress-test experiments in two ground-truth settings: three full cycles and three broken cycles. In the broken-cycle settings, at least one edge per cycle was attenuated to 0.1, below the noise level, thereby masking or partially disrupting cycles at the observation level. Figure 6 shows the three broken-cycle experiment in setting.

Results. Recovery accuracy was quantified using cosine similarity between the estimated and ground-truth edge flows [Luo et al., 2018, Zhao and Jia, 2025]. Cosine similarity is scale-invariant and measures directional agreement independently of magnitude, making it particularly suitable for evaluating cyclic recovery. Unlike edgewise accuracy, it remains sensitive to recovery of the underlying circulation even when individual edges are noisy or partially disrupted.

Tables 1–2 summarize results over 100 simulations. In the fully observed three-cycle network, all baseline methods achieved low cosine similarities (0.02–0.22), indicating poor recovery of the true cyclic organization. After har-

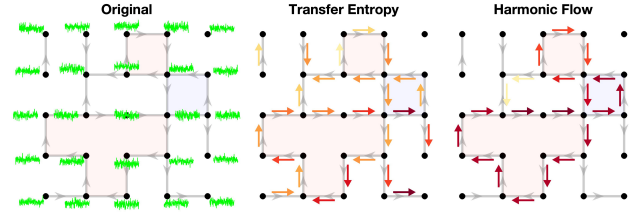


Figure 5: **Left:** Ground-truth directed edge flow on a cubical complex, consisting of two clockwise (red) and one counterclockwise (blue) circulations. Node time series are generated from a VAR-process driven by these prescribed edge flows. **Middle:** Directed interactions estimated using transfer entropy (colored arrows). Spurious signals appear along non-cyclic edges, obscuring the underlying cyclic organization. **Right:** Harmonic flow obtained via the Hodge projection of the transfer entropy. Color scales differ across panels because harmonic flow is the orthogonal projection of transfer entropy onto the cycle space and therefore has smaller magnitude.

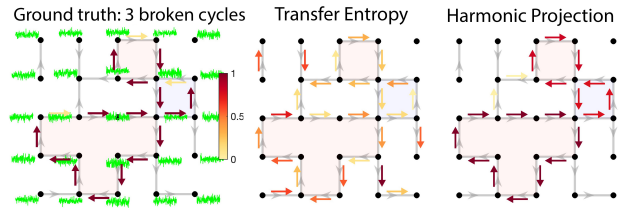


Figure 6: Simulation setting differ from Figure 5 example by introducing broken edges in cycles. One edge per cycle is weakened below the noise level, masking cyclic structure in the observations. Existing methods, including transfer entropy, fail to recover the cyclic organization, whereas harmonic projection recovers the underlying cycles.

monic projection, recovery increased substantially across all estimators, reaching approximately 0.79–0.83 regardless of noise level. Similar behavior was observed when one edge in each cycle was weakened below the noise level. While baseline methods again failed (0.02–0.23), harmonic projection maintained high recovery (0.72–0.75). Performance remained remarkably stable across noise levels $\sigma = 0.1, 1$, and 10, demonstrating robustness to both observation noise and partially broken cycles. These results indicate that harmonic projection recovers persistent cyclic organization even when individual cycle edges are weak, noisy, or missing in the observed interactions.

5 APPLICATION

Human Neural Networks. We applied the proposed framework to resting-state functional magnetic resonance imaging (rs-fMRI) data from 400 healthy young adults (age 22–36 years, mean 29.24 ± 3.39 years) drawn from the Human Connectome Project (HCP) [Van Essen et al., 2012].

Table 1: Cosine similarity (mean \pm s.d.) over 100 trials for recovering ground truth circulations under across different noise levels σ . The top block reports baseline methods, and the bottom block reports their harmonic projections. A cosine similarity of 1 indicates perfect recovery of the true cyclic flow. Three interacting-cycle network with full cyclic ground truth.

Method	Noise σ	Granger	SEM	Bayesian	Transfer Entropy	Lagged Corr.	NOTEARS	CCD
Baseline	0.10	0.19 \pm 0.02	0.17 \pm 0.03	0.17 \pm 0.03	0.21 \pm 0.01	0.21 \pm 0.05	0.02 \pm 0.04	0.03 \pm 0.05
	1.00	0.20 \pm 0.02	0.17 \pm 0.02	0.17 \pm 0.02	0.21 \pm 0.01	0.22 \pm 0.05	0.03 \pm 0.05	0.02 \pm 0.04
	10.0	0.19 \pm 0.02	0.17 \pm 0.02	0.17 \pm 0.03	0.21 \pm 0.01	0.21 \pm 0.05	0.02 \pm 0.04	0.02 \pm 0.05
Harmonic	0.10	0.82 \pm 0.01	0.80 \pm 0.02	0.79 \pm 0.03	0.83 \pm 0.00	0.79 \pm 0.00	–	–
	1.00	0.82 \pm 0.01	0.80 \pm 0.02	0.80 \pm 0.02	0.83 \pm 0.00	0.79 \pm 0.00	–	–
	10.0	0.82 \pm 0.01	0.79 \pm 0.03	0.79 \pm 0.03	0.83 \pm 0.00	0.79 \pm 0.00	–	–

Table 2: Three interacting-cycle simulation in which at least one edge in each cycle is broken.

Method	Noise σ	Granger	SEM	Bayesian	Transfer Entropy	Lagged Corr.	NOTEARS	CCD
Baseline	0.10	0.19 \pm 0.02	0.16 \pm 0.03	0.16 \pm 0.03	0.20 \pm 0.01	0.22 \pm 0.05	0.02 \pm 0.04	0.02 \pm 0.04
	1.00	0.19 \pm 0.02	0.17 \pm 0.02	0.16 \pm 0.02	0.20 \pm 0.01	0.22 \pm 0.05	0.03 \pm 0.04	0.03 \pm 0.06
	10.0	0.18 \pm 0.02	0.16 \pm 0.03	0.17 \pm 0.02	0.20 \pm 0.01	0.23 \pm 0.05	0.02 \pm 0.04	0.02 \pm 0.05
Harmonic	0.10	0.74 \pm 0.01	0.72 \pm 0.03	0.72 \pm 0.03	0.75 \pm 0.00	0.73 \pm 0.00	–	–
	1.00	0.74 \pm 0.01	0.72 \pm 0.02	0.72 \pm 0.02	0.75 \pm 0.00	0.73 \pm 0.00	–	–
	10.0	0.74 \pm 0.01	0.72 \pm 0.03	0.72 \pm 0.03	0.75 \pm 0.00	0.73 \pm 0.00	–	–

Resting-state fMRI measures spontaneous BOLD fluctuations as markers of neuronal activity [Huang et al., 2020, Liu et al., 2025], producing high-dimensional time series with complex network interactions suitable for evaluating cyclic structure.

For each subject, we analyzed 648 seconds (10.8 minutes) of data. Directed edge flows were estimated using time-lagged Pearson correlations computed within 20-second sliding windows advanced in 5-second increments [Huang et al., 2020, Keilholz et al., 2017, Petri et al., 2014]. The window length captures lagged dependencies while preserving temporal variation in interaction structure [Keilholz et al., 2017]. The window length was chosen to cover the main temporal extent of the BOLD hemodynamic response: the response typically begins after approximately 1–2 seconds, peaks around 4–6 seconds, and can exhibit an undershoot over approximately 10–20 seconds [Glover, 1999]. Thus, a 20-second window provides a practical short-window scale for estimating time-resolved rs-fMRI connectivity while retaining sufficient temporal localization. For each node pair, the dominant lagged correlation defined the directed interaction.

Failure of Direct Averaging. Due to inter-subject variability and temporal asynchrony, direct averaging of time-varying edge flows largely cancels directional effects, producing extremely weak mean connectivity (maximum correlation = 0.034 in Figure 7, left). The Rayleigh test [Mardia and Jupp, 2009] yields a p-value of 0.50, indicating no coherent population-level alignment.

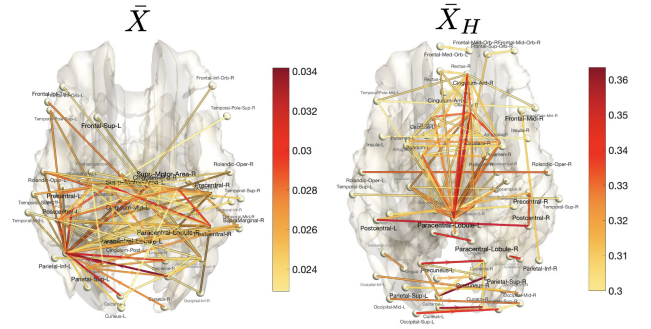


Figure 7: **Left:** Average edge flow \bar{X} over time and subjects derived from time-lagged Pearson correlations. The mean edge magnitudes are small (approximately 0.02–0.034) and statistically insignificant ($p = 0.50$); no edge exceeds a correlation of 0.3. Here we display the 100 largest edges, all of which remain statistically insignificant. **Right:** Average harmonic flow \bar{X}_H over time and subjects computed from the same time-lagged correlations, which are highly significant ($p < 10^{-29}$). The 100 largest harmonic edges (with magnitudes all above 0.3) are shown.

This reflects a fundamental challenge in resting-state network analysis: time-resolved functional connectivity is not temporally synchronized across subjects or across time [Huang et al., 2020]. Transient correlations fluctuate in both sign and magnitude, so direct averaging of dynamic directed networks is *ill-posed*; opposing directional patterns cancel, obscuring recurrent structure. Consequently, many prior studies rely on static connectivity summaries, sacrificing

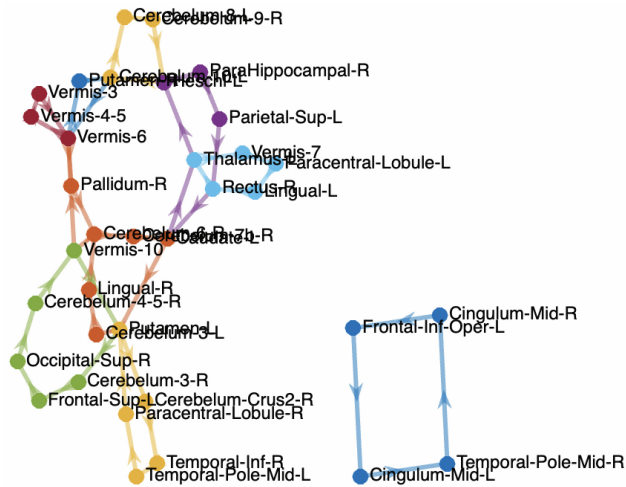


Figure 8: Top 10 cycles out of 534 identified from the mean harmonic flow \bar{U} across 400 human brain networks ($p < 10^{-29}$). The cycles repeatedly involve shared brain regions but not identical directed edges, indicating reproducible cyclic organization at the node level rather than exact edgewise recurrence. This explains why direct edge-weight averaging fails to align cycles.

temporal and directional information [Huang et al., 2020, Ma et al., 2023].

At the same time, large-scale neural systems exhibit recurrent and feedback-driven dynamics [Deco et al., 2013, Liu et al., 2025]. Yet most brain network methods impose acyclicity or focus on feedforward dependencies [Peters et al., 2017, Weichwald and Peters, 2021, Zheng et al., 2018], excluding cyclic interactions as primary organizational principles. This mismatch limits the ability of existing models to identify persistent recurrent structure and motivates frameworks that explicitly target cyclic interactions. The proposed harmonic flow offers a principled and structurally grounded resolution to this longstanding challenge.

Results. Despite the absence of explicit tasks, the population-level harmonic flow \bar{X}_H , obtained by averaging across subjects and time, exhibits a structured and temporally stable organization. This stability enables meaningful aggregation of dynamic networks across individuals and time windows (Figure 7, right), in contrast to conventional time-resolved connectivity measures, which largely cancel under averaging. A Rayleigh test applied to the averaged harmonic flow yields $p < 10^{-29}$, indicating exceptionally strong population-level cyclic alignment.

At the group level, the harmonic component reveals a small number of large-scale recurrent cycles that persist across subjects. These cycles link bilaterally symmetric sensory and motor cortices with midline structures, forming recurrent loops consistent with coordinated interhemispheric processing. The resulting anatomically interpretable patterns

indicate that harmonic flow captures intrinsic functional symmetries and stable feedback pathways that are difficult to recover using acyclic models or static connectivity averages.

6 CONCLUSION

We introduced a variational formulation for directed interactions based on dissipative Lagrangian dynamics. Unlike DAG-based approaches that exclude or relax cycles, the proposed framework treats recurrence as a primary structure of interest. In the strongly dissipative regime, the dynamics converge to a harmonic steady state that isolates the stable cyclic component determined by network topology. Thus cycles are not imposed structurally, but emerge as the asymptotic limit of the dissipative dynamics.

Applied to dynamic human neural networks, raw directed edge flows largely cancel under averaging, whereas harmonic projection reveals strong and reproducible group-level cyclic organization. This suggests that recurrence manifests as stable global alignment rather than as large marginal edge effects. By selecting the harmonic component through variational dynamics, the framework provides a principled mechanism for identifying cyclic structure as the intrinsic stable limit of dissipative dynamics in feedback-dominated systems.

References

- L. Ambrosio, N. Gigli, and G. Savaré. *Gradient flows: in metric spaces and in the space of probability measures*. Springer, 2005.
- D.V. Anand and M.K. Chung. Hodge-Laplacian of brain networks. *IEEE Transactions on Medical Imaging*, 42: 1563–1573, 2023.
- D.V. Anand and M.K. Chung. Hodge-decomposition of brain networks. In *2024 IEEE International Symposium on Biomedical Imaging (ISBI)*, pages 1–5. IEEE, 2024.
- A. Arenas, A. Díaz-Guilera, J. Kurths, Y. Moreno, and C. Zhou. Synchronization in complex networks. *Physics Reports*, 469(3):93–153, 2008.
- V.I. Arnol’d. *Mathematical methods of classical mechanics*, volume 60. Springer, 2013.
- L. Barnett and A.K. Seth. The MVGC multivariate Granger causality toolbox: A new approach to granger-causal inference. *Journal of Neuroscience Methods*, 223:50–68, 2014.
- S. Bongers, P. Forré, J. Peters, and J.M. Mooij. Foundations of structural causal models with cycles and latent variables. *The Annals of Statistics*, 49:2885–2915, 2021.

- Miles C., Sam G., Stephan H., Peter B., David S., and Shirley H. Lagrangian neural networks. In *ICLR 2020 Workshop on Integration of Deep Neural Models and Differential Equations*, 2019.
- G. Casella and R. Berger. *Statistical Inference*. Chapman and Hall/CRC, 2024.
- F.R.K. Chung and S.T. Yau. Eigenvalue inequalities for graphs and convex subgraphs. *Communications in Analysis and Geometry*, 5:575–624, 1997.
- M.K. Chung, H. Lee, A. DiChristofano, H. Ombao, and V. Solo. Exact topological inference of the resting-state brain networks in twins. *Network Neuroscience*, 3:674–694, 2019.
- M.K. Chung, L. Maccotta, and A. Struck. Counterfactual analysis of brain network dynamics. In *Proceedings of the IEEE International Symposium on Biomedical Imaging (ISBI)*, pages 1–5, 2026.
- Y.-M. Chung, C.-S. Hu, E. Sun, and H.C. Tseng. Morphological multiparameter filtration and persistent homology in mitochondrial image analysis. *Plos one*, 19:e0310157, 2024.
- P. Dayan and L.F. Abbott. *Theoretical neuroscience: computational and mathematical modeling of neural systems*. 2005.
- G. Deco, V.K. Jirsa, and A.R. McIntosh. Resting brains never rest: computational insights into potential cognitive architectures. *Trends in Neurosciences*, 36(5):268–274, 2013.
- C.C. Driver, J.H.L. Oud, and M.C. Voelkle. Continuous time structural equation modeling with R package ctsem. *Journal of Statistical Software*, 77:1–35, 2017.
- H. Edelsbrunner and J. Harer. *Computational topology: An introduction*. American Mathematical Society, 2010.
- K. Fan. On a theorem of Weyl concerning eigenvalues of linear transformations i. *Proceedings of the National Academy of Sciences*, 35:652–655, 1949.
- P. Forré and J.M. Mooij. Constraint-based causal discovery for non-linear structural causal models with cycles and latent founders. In *Proceedings of the 34th Conference on Uncertainty in Artificial Intelligence (UAI)*, pages 952–961, 2018.
- G.H. Glover. Deconvolution of impulse response in event-related BOLD fmri1. *Neuroimage*, 9:416–429, 1999.
- H. Goldstein. *Classical Mechanics*. Addison-Wesley, Reading, MA, 1950.
- C. Gong, C. Zhang, D. Yao, J. Bi, W. Li, and Y. Xu. Causal discovery from temporal data: An overview and new perspectives. *ACM Computing Surveys*, 57(4):1–38, 2024.
- C.W.J. Granger. Investigating causal relations by econometric models and cross-spectral methods. *Econometrica: Journal of the Econometric Society*, pages 424–438, 1969.
- S. Greydanus, M. Dzamba, and J. Yosinski. Hamiltonian neural networks. In *Advances in Neural Information Processing Systems*, volume 32, 2019.
- Allen Hatcher. *Algebraic topology*. Cambridge University Press, 2002.
- R. Horn and C. Johnson. *Matrix Analysis*. Cambridge University Press, London, 1985.
- S.-G. Huang, S.-T. Samdin, C.M. Ting, H. Ombao, and M.K. Chung. Statistical model for dynamically-changing correlation matrices with application to brain connectivity. *Journal of Neuroscience Methods*, 331:108480, 2020.
- D.B. Johnson. Finding all the elementary circuits of a directed graph. *SIAM Journal on Computing*, 4:77–84, 1975.
- S. Keilholz, C. Caballero-Gaudes, P. Bandettini, G. Deco, and V. Calhoun. Time-resolved resting-state functional magnetic resonance imaging analysis: current status, challenges, and new directions. *Brain Connectivity*, 7:465–481, 2017.
- L. Kilian and H. Lütkepohl. *Structural vector autoregressive analysis*. Cambridge University Press, 2017.
- G. Lacerda, Peter S., J. Ramsey, and P.O. Hoyer. Discovering cyclic causal models by independent components analysis. In *Proceedings of the 24th Conference on Uncertainty in Artificial Intelligence (UAI)*, pages 366–374, 2008.
- H. Lee, Kang H. Chung, M.K., and D.S. Lee. Hole detection in metabolic connectivity of Alzheimer’s disease using k-Laplacian. *MICCAI, Lecture Notes in Computer Science*, 8675:297–304, 2014.
- L.-H. Lim. Hodge laplacians on graphs. *Siam Review*, 62: 685–715, 2020.
- Z.-Q. Liu, A.I. Luppi, J.Y. Hansen, Y.E. Tian, A. Zalesky, B.T.T. Yeo, B.D. Fulcher, and B. Misic. Benchmarking methods for mapping functional connectivity in the brain. *Nature Methods*, pages 1–10, 2025.
- C. Luo, J. Zhan, X. Xue, L. Wang, R. Ren, and Q. Yang. Cosine normalization: Using cosine similarity instead of dot product in neural networks. In *International Conference on Artificial Neural Networks*, pages 382–391, 2018.

- H. Lütkepohl. *New Introduction to Multiple Time Series Analysis*. Springer, Berlin, 2005.
- Michael Lutter, Christian Ritter, and Jan Peters. Deep Lagrangian networks: Using physics as model prior for deep learning. In *International Conference on Learning Representations*, 2019.
- Y. Ma, Q. Wang, L. Cao, L. Li, C. Zhang, L. Qiao, and M. Liu. Multi-scale dynamic graph learning for brain disorder detection with functional MRI. *IEEE Transactions on Neural Systems and Rehabilitation Engineering*, 31: 3501–3512, 2023.
- K.V. Mardia and P.E. Jupp. *Directional Statistics*. John Wiley & Sons, 2009.
- M. Mesbahi and M. Egerstedt. Graph theoretic methods in multiagent networks. 2010.
- J.M. Mooij, D. Janzing, T. Heskes, and B. Schölkopf. From ordinary differential equations to structural causal models: The deterministic case. In *Proceedings of the 29th Conference on Uncertainty in Artificial Intelligence (UAI)*, pages 440–448, 2013.
- M. Noirhomme, E. Opsomer, and N. Vandewalle. Onsager variational principle for granular fluids. *Physical Review E*, 110:054901, 2024.
- R. Olfati-Saber, J. A. Fax, and R. M. Murray. Consensus and cooperation in networked multi-agent systems. *Proceedings of the IEEE*, 2007.
- A. Papan, C. Kyrtsov, D. Kugiumtzis, and C. Diks. Financial networks based on Granger causality: A case study. *Physica A: Statistical Mechanics and its Applications*, 482:65–73, 2017.
- J. Pearl. *Causality: Models, Reasoning, and Inference*. Cambridge University Press, Cambridge, UK, 2 edition, 2009.
- J. Peters, D. Janzing, and B. Schölkopf. *Elements of causal inference: foundations and learning algorithms*. MIT press, Cambridge, MA, 2017.
- G. Petri, P. Expert, F. Turkheimer, R. Carhart-Harris, D. Nutt, P.J. Hellyer, and F. Vaccarino. Homological scaffolds of brain functional networks. *Journal of The Royal Society Interface*, 11:20140873, 2014.
- G.E. Primiceri. Time varying structural vector autoregressions and monetary policy. *The Review of Economic Studies*, 72:821–852, 2005.
- T.S. Richardson. A discovery algorithm for directed cyclic graphs. *Proceedings of the 12th International Conference on Uncertainty in Artificial Intelligence*, 1996.
- M.T. Schaub, A.R. Benson, P. Horn, G. Lippner, and A. Jadbabaie. Random walks on simplicial complexes and the normalized Hodge 1-laplacian. *SIAM Review*, 62:353–391, 2020.
- T. Schreiber. Measuring information transfer. *Physical Review Letters*, 85:461, 2000.
- S.M. Smith, K.L. Miller, G. Salimi-Khorshidi, M. Webster, C.F. Beckmann, T.E. Nichols, J.D. Ramsey, and M.W. Woolrich. Network modelling methods for FMRI. *Neuroimage*, 54:875–891, 2011.
- P. Spirtes, C. N. Glymour, and R. Scheines. *Causation, Prediction, and Search*. MIT Press, Cambridge, MA, 2 edition, 2000.
- O. Sporns, G. Tononi, and GM Edelman. Theoretical neuroanatomy: relating anatomical and functional connectivity in graphs and cortical connection matrices. *Cerebral Cortex*, 10:127, 2000.
- Z. Su, Y. Tong, and G.-W. Wei. Hodge decomposition of single-cell RNA velocity. *Journal of Chemical Information and Modeling*, 64:3558–3568, 2024.
- R. Tarjan. Depth-first search and linear graph algorithms. *SIAM Journal on Computing*, 1:146–160, 1972.
- D.C. Van Essen, K. Ugurbil, E. Auerbach, D. Barch, T.E.J. Behrens, R. Bucholz, A. Chang, L. Chen, M. Corbetta, and S.W. Curtiss. The human connectome project: a data acquisition perspective. *NeuroImage*, 62:2222–2231, 2012.
- Van V.C. and H. Sompolinsky. Chaos in neuronal networks with balanced excitatory and inhibitory activity. *Science*, 274(5293):1724–1726, 1996.
- S. Weichwald and J. Peters. Causality in cognitive neuroscience: concepts, challenges, and distributional robustness. *Journal of Cognitive Neuroscience*, 33(2):226–247, 2021.
- Y. Zhao and J. Jia. DAGSLAM: causal Bayesian network structure learning of mixed type data and its application in identifying disease risk factors. *BMC Medical Research Methodology*, 25:154, 2025.
- X. Zheng, B. Aragam, P.K. Ravikumar, and E.P. Xing. Dags with no tears: Continuous optimization for structure learning. *Advances in Neural Information Processing Systems*, 31, 2018.

A PROOFS TO THEOREMS

Theorem 5 (Euler–Lagrange dynamics). *An edge-flow trajectory $X(t)$ is a stationary point of the action functional*

$\mathcal{A}[X]$ if and only if it satisfies the Euler–Lagrange equation

$$\ddot{X}(t) + \Delta_1 X(t) = 0.$$

Proof. Consider a perturbed edge-flow trajectory $X_\varepsilon(t) = X(t) + \varepsilon\eta(t)$, where the perturbation $\eta : [0, 1] \rightarrow \mathbb{R}^{|E|}$ is smooth and satisfies the boundary conditions $\eta(0) = 0$, $\eta(1) = 0$ and nonzero only inside $(0, 1)$. The corresponding action is

$$\mathcal{A}[X_\varepsilon] = \int_0^\infty \mathcal{L}(X_\varepsilon(t), \dot{X}_\varepsilon(t)) dt.$$

The action associated with this perturbed trajectory is

$$\mathcal{A}[X_\varepsilon] = \frac{1}{2} \int_0^\infty \|\dot{X} + \varepsilon\dot{\eta}\|_2^2 - (X + \varepsilon\eta)^\top \Delta_1 (X + \varepsilon\eta) dt.$$

Differentiating with respect to ε at $\varepsilon = 0$ gives

$$\delta\mathcal{A}[X_\varepsilon] = \left. \frac{d}{d\varepsilon} \mathcal{A}[X_\varepsilon] \right|_{\varepsilon=0} = \int_0^\infty \left(\dot{X}^\top \dot{\eta} - \eta^\top \Delta_1 X \right) dt,$$

where we used the symmetry of Δ_1 to simplify the second term. Integration by parts gives

$$\int_0^\infty \dot{X}^\top \dot{\eta} dt = [\dot{X}^\top \eta]_0^\infty - \int_0^\infty \ddot{X}^\top \eta dt.$$

The boundary term vanishes because $\eta(0) = 0$ and $\eta(t) = 0$ for sufficiently large t . Subsequently,

$$\delta\mathcal{A}[X_\varepsilon] = - \int_0^\infty \eta(t)^\top (\ddot{X}(t) + \Delta_1 X(t)) dt. \quad (4)$$

The variation must be zero for every choice of perturbation $\eta(t)$. Thus,

$$\ddot{X}(t) + \Delta_1 X(t) = 0,$$

which is the *Euler–Lagrange equation* [Arnol’d, 2013] governing the evolution of the edge flow. \square

Theorem 6 (Dissipative dynamics). *Edge flow $X(t)$ satisfies the Lagrange–d’Alembert principle if and only if it satisfies the damped Euler–Lagrange equation*

$$\ddot{X} + \gamma \dot{X} + \Delta_1 X = 0. \quad (5)$$

Proof. From variation (4) for Theorem 5,

$$\delta\mathcal{A}[X] = - \int_0^\infty \eta(t)^\top (\ddot{X}(t) + \Delta_1 X(t)) dt.$$

For Rayleigh dissipation, we have

$$- \int_0^\infty \langle F(t), \delta X(t) \rangle dt = \int_0^\infty \gamma \dot{X}(t)^\top \eta(t) dt,$$

with $\delta X(t) = \eta(t)$. Combining terms gives

$$\int_0^\infty \eta(t)^\top (\ddot{X}(t) + \gamma \dot{X}(t) + \Delta_1 X(t)) dt = 0.$$

Since this equality should hold for all admissible perturbations $\eta(t)$, the integral must vanish, yielding the damped Euler–Lagrange equation. The converse follows immediately by reversing the above steps. \square

Theorem 7 (Harmonic flows are cycles). *Every nonzero harmonic flow $X \in \ker(\Delta_1)$ consists of circulations around cycles of the simplicial complex.*

Proof. For any edge flow $X \in \mathbb{R}^{|E|}$, we have

$$\begin{aligned} \langle X, \Delta_1 X \rangle &= \langle X, \mathbf{B}_1^\top \mathbf{B}_1 X \rangle + \langle X, \mathbf{B}_2 \mathbf{B}_2^\top X \rangle \\ &= \langle \mathbf{B}_1 X, \mathbf{B}_1 X \rangle + \langle \mathbf{B}_2^\top X, \mathbf{B}_2^\top X \rangle \\ &= \|\mathbf{B}_1 X\|_2^2 + \|\mathbf{B}_2^\top X\|_2^2. \end{aligned}$$

If $X \in \ker(\Delta_1)$, then $\Delta_1 X = 0$ and hence

$$0 = \langle X, \Delta_1 X \rangle = \|\mathbf{B}_1 X\|_2^2 + \|\mathbf{B}_2^\top X\|_2^2.$$

Since both terms are nonnegative, each must vanish individually. Therefore $\mathbf{B}_1 X = 0$ and $\mathbf{B}_2^\top X = 0$, implying $X \in \ker(\mathbf{B}_1) \cap \ker(\mathbf{B}_2^\top)$.

Conversely, if $X \in \ker(\mathbf{B}_1) \cap \ker(\mathbf{B}_2^\top)$, then $\mathbf{B}_1 X = 0$ and $\mathbf{B}_2^\top X = 0$, which yields

$$\Delta_1 X = \mathbf{B}_1^\top (\mathbf{B}_1 X) + \mathbf{B}_2 (\mathbf{B}_2^\top X) = 0.$$

Thus $X \in \ker(\Delta_1)$.

Subsequently, $\mathbf{B}_1 X = 0$ and $\mathbf{B}_2^\top X = 0$. The condition $\mathbf{B}_1 X = 0$ means that, at every vertex, the signed sum of incident edge flows vanishes. Thus X has no net inflow or outflow at any vertex, and therefore forms a closed circulation, i.e., a 1-cycle in simplicial homology [Hatcher, 2002]. The additional condition $\mathbf{B}_2^\top X = 0$ removes components that can be written as boundaries of 2-simplices (filled-in triangles). Consequently, X represents circulation along cycles that are not boundaries of higher-dimensional faces.

If $X \neq 0$, at least one such cyclic component is nontrivial. \square

Theorem 8 (Variance reduction of harmonic flow). *Let $X \in \mathbb{R}^{|E|}$ be a random edge flow with isotropic covariance $\Sigma_X = \sigma^2 I$. Then the total variance of the harmonic flow $X_H = \mathcal{P}_H X$ satisfies*

$$\text{Var}(X_H) = \frac{\beta_1}{|E|} \text{Var}(X), \quad (6)$$

where $\beta_1 = \dim \ker(\Delta_1)$ is the first Betti number, equal to the dimension of the harmonic subspace.

Proof. By definition, the total variance of the edge flow is

$$\text{Var}(X) = \mathbb{E}\|X - \bar{X}\|_2^2 = \text{tr}(\Sigma_X).$$

Under the isotropic assumption $\Sigma_X = \sigma^2 I$, this becomes

$$\text{Var}(X) = \text{tr}(\sigma^2 I) = |E| \sigma^2.$$

The harmonic flow is obtained by orthogonal projection,

$$X_H = \mathcal{P}_H X,$$

where \mathcal{P}_H is symmetric and idempotent, i.e., $\mathcal{P}_H^\top = \mathcal{P}_H$ and $\mathcal{P}_H^2 = \mathcal{P}_H$. The covariance of X_H is therefore

$$\Sigma_H = \mathbb{E}[(X_H - \mathbb{E}X_H)(X_H - \mathbb{E}X_H)^\top] = \mathcal{P}_H \Sigma_X \mathcal{P}_H.$$

Substituting $\Sigma_X = \sigma^2 I$ yields

$$\Sigma_H = \sigma^2 \mathcal{P}_H.$$

The total variance of the harmonic flow is then

$$\text{Var}(X_H) = \text{tr}(\Sigma_H) = \sigma^2 \text{tr}(\mathcal{P}_H).$$

Since \mathcal{P}_H is an orthogonal projector, its trace equals its rank, which is the dimension of the harmonic subspace:

$$\text{tr}(\mathcal{P}_H) = \text{rank}(\mathcal{P}_H) = \dim \ker(\Delta_1) = \beta_1.$$

Hence,

$$\text{Var}(X_H) = \sigma^2 \beta_1$$

and obtain the result. \square

Theorem 9 (Variance bounds for harmonic flow). *Let $X \in \mathbb{R}^{|E|}$ be a random edge flow with nonnegative definite covariance $\Sigma_X \succeq 0$, and let $\sigma_1 \geq \sigma_2 \geq \dots \geq \sigma_{|E|} \geq 0$ denote the eigenvalues of Σ_X .*

$$\frac{\sum_{i=|E|-\beta_1+1}^{|E|} \sigma_i}{\sum_{i=1}^{|E|} \sigma_i} \leq \frac{\text{Var}(X_H)}{\text{Var}(X)} \leq \frac{\sum_{i=1}^{\beta_1} \sigma_i}{\sum_{i=1}^{|E|} \sigma_i}. \quad (7)$$

The upper bound is attained when the harmonic subspace aligns with the top β_1 eigenvectors of Σ_X , and the lower bound when it aligns with the bottom β_1 eigenvectors.

Proof. Let the spectral decomposition of Σ_X be

$$\Sigma_X = \sum_{i=1}^{|E|} \sigma_i u_i u_i^\top, \quad \sigma_1 \geq \sigma_2 \geq \dots \geq \sigma_{|E|} \geq 0,$$

where $\{u_i\}_{i=1}^{|E|}$ forms an orthonormal basis of eigenvectors.

The total variance of X is

$$\text{Var}(X) = \mathbb{E}\|X - \bar{X}\|_2^2 = \text{tr}(\Sigma_X) = \sum_{i=1}^{|E|} \sigma_i.$$

The covariance of the harmonic flow $X_H = \mathcal{P}_H X$ is

$$\Sigma_H = \mathbb{E}[\mathcal{P}_H(X - \bar{X})(X - \bar{X})^\top \mathcal{P}_H] = \mathcal{P}_H \Sigma_X \mathcal{P}_H.$$

Therefore, the total variance of X_H is

$$\text{Var}(X_H) = \text{tr}(\Sigma_H) = \text{tr}(\Sigma_X \mathcal{P}_H),$$

using the fact that \mathcal{P}_H is symmetric and idempotent, i.e., $\mathcal{P}_H^2 = \mathcal{P}_H$ and $\mathcal{P}_H^\top = \mathcal{P}_H$.

Let $\{\psi_j\}_{j=1}^{\beta_1}$ be an orthonormal basis of $\ker(\Delta_1)$. Since \mathcal{P}_H is the orthogonal projector onto $\ker(\Delta_1)$, it admits the spectral representation

$$\mathcal{P}_H = \sum_{j=1}^{\beta_1} \psi_j \psi_j^\top.$$

Thus,

$$\text{Var}(X_H) = \text{tr}\left(\Sigma_X \sum_{j=1}^{\beta_1} \psi_j \psi_j^\top\right) = \sum_{j=1}^{\beta_1} \psi_j^\top \Sigma_X \psi_j,$$

which is a Rayleigh sum of Σ_X over the β_1 -dimensional harmonic subspace [Horn and Johnson, 1985]. By Ky Fan's inequality [Fan, 1949], we have

$$\sum_{i=|E|-\beta_1+1}^{|E|} \sigma_i \leq \sum_{j=1}^{\beta_1} \psi_j^\top \Sigma_X \psi_j \leq \sum_{i=1}^{\beta_1} \sigma_i$$

and obtain the result. \square